2011

# Thermographic signal reconstruction for vibrothermography

Stephen D. Holland
*Iowa State University*, sdh4@iastate.edu

# Thermographic signal reconstruction for vibrothermography

**Abstract**
Vibrothermography, also known as thermosonics or sonic infrared, is a method of nondestructive evaluation that finds cracks or delaminations from the heat given off in response to vibration. In vibrothermography, finding cracks requires identifying and localizing pulsed surface and subsurface heat sources from a time sequence of infrared images. Traditionally this identification involves manually stepping through and studying the images. Careful observation of the heating and subsequent cooling is needed to distinguish cracks from false indications. In this paper, we present an algorithm that reduces the entire time sequence to a single static plot. The plot uses only a few coefficients per pixel to reconstruct the original sequence; this is possible because the reduction is based on a physical model. As an added bonus, the algorithm reduces noise and improves sensitivity. A single false-color image summarizes all the information from the entire sequence, simplifying the task of identifying cracks.

**Keywords**
Vibrothermography, Sonic Infrared, Sonic IR, image processing, physics-based image analysis, heat conduction, nondestructive testing, nondestructive evaluation

**Disciplines**
Aerospace Engineering

**Comments**
This is a post-print of an article from *Infrared Physics & Technology*, 54, no. 6 (November 2011): 503–511, doi: 10.1016/j.infrared.2011.07.004.

# Thermographic signal reconstruction for vibrothermography

Stephen D. Holland*,[a]

[a]*Department of Aerospace Engineering and Center for Nondestructive Evaluation*
*Iowa State University*
*1915 Scholl Road*
*Ames, IA 50011*

**Abstract**

Vibrothermography, also known as thermosonics or sonic infrared, is a method of nondestructive evaluation that finds cracks or delaminations from the heat given off in response to vibration. In vibrothermography, finding cracks requires identifying and localizing pulsed surface and subsurface heat sources from a time sequence of infrared images. Traditionally this identification involves manually stepping through and studying the images. Careful observation of the heating and subsequent cooling is needed to distinguish cracks from false indications. In this paper, we present an algorithm that reduces the entire time sequence to a single static plot. The plot uses only a few coefficients per pixel to reconstruct the original sequence; this is possible because the reduction is based on a physical model. As an added bonus, the algorithm reduces noise and improves sensitivity. A single false-color image summarizes all the information from the entire sequence, simplifying the task of identifying cracks.

*Key words:* Vibrothermography, Sonic Infrared, Sonic IR, image processing, physics-based image analysis, heat conduction

## 1. Introduction

Vibrothermography [1], also known as thermosonics [2] and sonic infrared (Sonic IR) [3], is a method of nondestructive evaluation that finds cracks or

*Corresponding author
*Email address:* sdh4@iastate.edu (Stephen D. Holland)

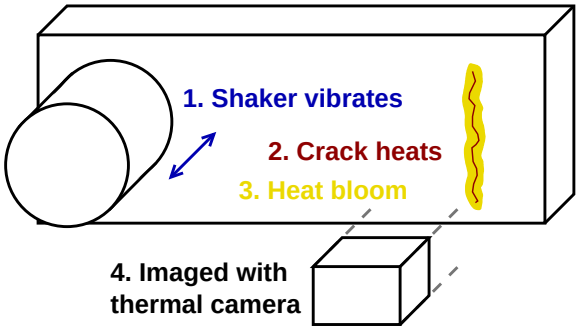


Figure 1: The vibrothermography process: 1. Vibration is generated by a sonic or ultrasonic shaker. 2. Any crack in the specimen will generate heat. 3. This heat will bloom and diffuse outwards. 4. A thermal camera records a sequence of images showing the heating and diffusion.

delaminations from the heat they give off in response to vibration [4]. The vibrothermography process is illustrated in Fig. 1. A sonic or ultrasonic shaker vibrates the specimen for a short period of time (1-2 s). If a crack is present, its surfaces will rub against each other, generating heat. This heat then conducts outward. The temperature change is recorded as a movie (sequence of images) with a thermal camera. The diffusive nature of heat conduction means that the crack indications in the thermal images are inherently blurred and indistinct. Finding a crack with vibrothermography requires interpreting the thermal image sequence to identify the characteristic bloom [5] of the heat diffusion. This bloom distinguishes crack heating from other causes of apparent temperature change, such as reflections of heat sources in the environment.

Compared with other forms of thermography, relatively little has been published about image analysis for vibrothermography. The industrial need to find cracks, combined with the inherent difficulties due to information loss from the diffusive heat conduction and unknown source geometries, has led to a focus on detection over analysis. Background subtraction [6] is a near universal preprocessing step that removes the ambient temperature and any reflections from the thermal image. To transform an image or image sequence into a number representing a temperature rise, practitioners sometimes use algorithms such as local pixel averaging [7] or in our case surface fitting [8]. Various image enhancement techniques [4, 9] can be used to improve resolution or sharpness at the price of sensitivity, but such a tradeoff is antithetical

to the usual goal of maximizing crack detectability.

Matched filtering, based on the heat blooms that are observed around real indications, can be used to enhance detectability and improve discrimination of real cracks [5]. An industrial research group at Siemens has reported [10, 11] the use of pulse-phase analysis [12] to process vibrothermography image sequences, including the generation of a single-image summary that is superficially similar to the processed summary image presented here.

This paper describes a method for condensing a vibrothermography thermal image sequence into a single static plot that contains just six coefficients per pixel (four of which are of secondary significance). Such a small representation is possible because the method is based on a physical model of heat conduction. It retains the information needed to reconstruct the original thermal image sequence but rejects noise, thereby improving sensitivity. The condensed plot can be transformed into a manually interpretable summary image. It is also appropriate for direct input to an automatic pattern recognition algorithm.

Curve-fit based analysis and reconstruction of thermal image sequences is an established technique and widely used for analysis of thermal images from pulsed (flash) thermography [13]. This technique is known as thermographic signal reconstruction. While the details vary between practitioners, in general the cool-down curve after a thermal pulse is approximated by fitting to either a polynomial or a more constrained physically-motivated basis function. The curve fitting process both reduces noise (by not fitting to it), and compresses the useful information from the image sequence, reducing storage costs and allowing faster analysis.

In the vibrothermography process, uniform vibration (a tone burst) turns on at time $t_1$ and off at $t_2$, causing the crack to generate subsurface heat; the heat then diffuses to the surface, where the temperature can be measured over time by a thermal camera. The image sequence gathered by the thermal camera captures the surface temperature while the material warms and then cools as the heat is conducted away. Each pixel in the sequence of infrared images provides the temperature-time profile of a single point on the specimen surface. A number of synthetic temperature-time profiles are illustrated in Fig. 2.

The physics of heat conduction constrains the shape of the temperature profiles. Three possible (distance dependent) shapes can be derived analytically: Conduction of heat from a point source into a 3D volume (3D conduction), conduction of heat from a line source (2D conduction), and conduction

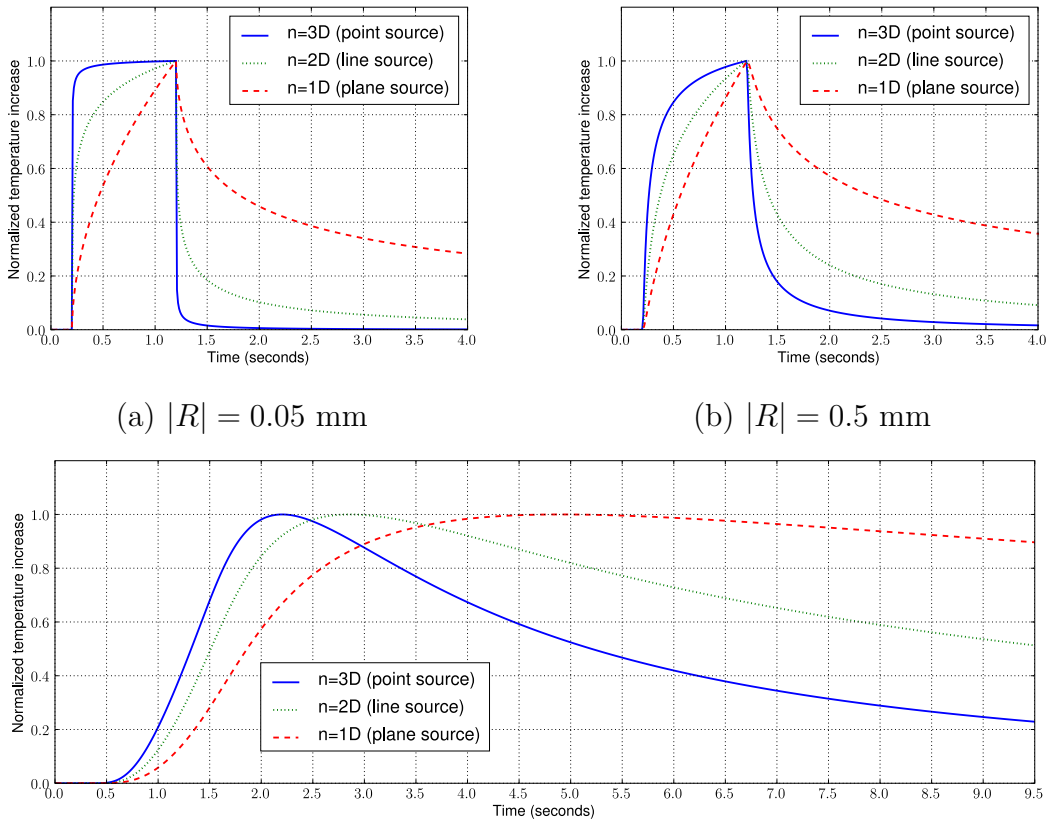


(a) $|R| = 0.05$ mm

(b) $|R| = 0.5$ mm

(c) $|R| = 5$ mm

Figure 2: Numerical calculations of heating profiles from a point, line, or plane source at a distance $|R|$ from the measurement point (a) $|R| = .05$ mm, (b) $|R| = .5$ mm, and (c) $|R| = 5$ mm. Thermal diffusivity $\alpha = 3 \times 10^{-6}$ m$^2$/s (approximate value for titanium). These curves represent theoretical heat-up and cool-down curves for a source turned on at time $t_1 = 0.2$ s, and off at time $t_2 = 1.2$ s.

of heat from a planar source (1D conduction). The method described in this paper relies on the observation that all three shapes share a common character, and on the assumption that they, to a reasonable approximation, span the space of possible temperature profiles.

## 2. Theory

Vibrothermographic crack heating occurs wherever the crack surfaces are in contact, but not closed so tightly as to lock the surfaces with static friction [14]. The heating zone could be a point, a line or arc, a surface, or anywhere in between.

The Green's function for $n-$dimensional heat diffusion (conduction) represents the influence of an impulse heat source at $t = \tau$ on the measured temperature a distance $|\underline{R}|$ away from the source [15],

$$T = \frac{1}{[4\pi\alpha(t-\tau)]^{n/2}} \exp\left(-\frac{|\underline{R}|^2}{4\alpha(t-\tau)}\right) \quad (t > \tau), \tag{1}$$

where $\alpha$ is the thermal diffusion coefficient, and $T$ is proportional to the increase of temperature at the measurement point at time $t$. Usually a temperature will be measured (with the thermal camera) at the material surface some lateral and vertical distance away from the heat source. A point heat source conducting into a 3D volume corresponds to $n = 3D$ heat conduction. A line source corresponds to $n = 2D$ conduction, and a plane source corresponds to $n = 1D$ conduction. Most real sources will not be perfect points, lines, or planes, but these three types of conduction span much of the range of possible sources. For example, consider the half-penny shaped surface crack illustrated in Fig. 3. This crack is presumed to be heating over its entire surface. Heat conduction near the center of the crack would be approximately one dimensional ($n$ = 1D), near the tips heat flow would be two dimensional ($n$ = 2D), and far enough away would become three dimensional ($n$ = 3D). In reality, the heat flow will always be somewhere between these three cases. Also, instead of a single distance $|R|$ there is a range of distances between any given measurement point and the locations where the crack transduces vibrational energy into heat. The diffusive nature of heat conduction suggests that it is not unreasonable to approximate the effect of different spatial extents of the source by the gross differences between 1D, 2D, and 3D heat conduction. The heating temperature profiles for n=1D,

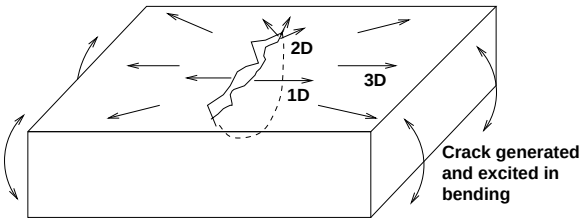


Figure 3: Diagram of a half-penny shaped crack. If the crack heats over its entire surface, heat conduction near the center will be one-dimensional ($n$ = 1D), whereas conduction near the tip will be two-dimensional ($n$ = 2D). Conduction farther away will be three dimensional ($n$ = 3D).

n=2D, and n=3D conduction turn out to be quite similar, and we will use those three cases to approximate the full spectrum of heating profiles.

The usual approach to Green's function-based prediction is to assume a source distribution and diffusivity $\alpha$, and then calculate the expected time-temperature sequence by convolving the source distribution with the Green's function Eq. 1 in space and time. For experiments with stationary tone-burst vibrational excitation the crack heating steps on at the turn-on time $t_1$, continues uniformly, then steps off at the turn-off time $t_2$.

Assume a buried point, line, or plane heat source, switched on from time $t_1$ to time $t_2$ and surrounded by a medium conducting heat away. The temperature at a distance $|R|$ from the source can be predicted from a convolution of Eq. 1 with the stepped on/off heat-source function for dimensionality $n$ of 1, 2, or 3:

$$T(t) = \begin{cases} 0 & (t \le t_1) \\ \int_{t_1}^{t} \frac{1}{[4\pi\alpha(t-\tau)]^{n/2}} \exp\left(-\frac{|R|^2}{4\alpha(t-\tau)}\right) d\tau & (t_1 < t \le t_2) \\ \int_{t_1}^{t_2} \frac{1}{[4\pi\alpha(t-\tau)]^{n/2}} \exp\left(-\frac{|R|^2}{4\alpha(t-\tau)}\right) d\tau & (t > t_2), \end{cases} \tag{2}$$

where multiplication by the stepped on/off function has been replaced by bounds on the integration.

The integrals in Eq. 2 can be evaluated (for example with computer algebra [16]) in terms of transcendental functions to form the expressions shown in table 1 for $n$ = 1 to 3 dimensional heat conduction. These expressions represent the range of possible heating vs. time profiles. Numerical evaluations of the expressions in table 1, normalized to unit peak with turn-on

$$
\begin{aligned}
T(t) &= 0 && (t \le t_1) \\
T(t) &= \frac{1}{4\pi\alpha|R|}\left[\operatorname{erfc}\left(\frac{|R|}{\sqrt{4\alpha(t-t_1)}}\right)\right] && (n=3 \text{ and } t_1 < t \le t_2) \\
T(t) &= \frac{1}{4\pi\alpha|R|}\left[\operatorname{erfc}\left(\frac{|R|}{\sqrt{4\alpha(t-t_1)}}\right) - \operatorname{erfc}\left(\frac{|R|}{\sqrt{4\alpha(t-t_2)}}\right)\right] && (n=3 \text{ and } t > t_2) \\
T(t) &= \frac{1}{4\pi\alpha}\left[-\operatorname{Ei}\left(-\frac{|R|^2}{4\alpha(t-t_1)}\right)\right] && (n=2 \text{ and } t_1 < t \le t_2) \\
T(t) &= \frac{1}{4\pi\alpha}\left[-\operatorname{Ei}\left(-\frac{|R|^2}{4\alpha(t-t_1)}\right) + \operatorname{Ei}\left(-\frac{|R|^2}{4\alpha(t-t_2)}\right)\right] && (n=2 \text{ and } t > t_2) \\
T(t) &= \frac{|R|}{4\alpha\sqrt{\pi}}\left[\Gamma\left(-0.5, -\frac{|R|^2}{4\alpha(t-t_1)}\right)\right] && (n=1 \text{ and } t_1 < t \le t_2) \\
T(t) &= \frac{|R|}{4\alpha\sqrt{\pi}}\left[\Gamma\left(-0.5, -\frac{|R|^2}{4\alpha(t-t_1)}\right) - \Gamma\left(-0.5, \frac{|R|^2}{4\alpha(t-t_2)}\right)\right] && (n=1 \text{ and } t > t_2)
\end{aligned}
$$

Table 1: Evaluations of integral of Eq. 2 for $n = 3, 2, 1$. $\operatorname{erfc}(x)$ represents the complementary error function, $\operatorname{Ei}(x)$ represents the exponential integral function, and $\Gamma(a, x)$ represents the upper incomplete gamma function. These expressions represent the heating a distance R away from a point, line, or plane heat source respectively that turns on at $t_1$ and off at $t_2$.

time $t_1 = 0.2$ s, turn-off time $t_2 = 1.2$ s, $\alpha = 3 \times 10^{-6}$ m$^2$/s, and at distances $|R| = .05$, 0.5, and 5 mm are shown in Figs. 2a, 2b, and 2c respectively.

All the heating profiles plotted in Fig. 2 – and indeed all possible heating vs. time profiles – share a common character: They all start at zero at $t_1 = 0.2$ s, increase to a peak at or shortly after $t_2 = 1.2$ s and then asymptotically return to zero. The characteristic diffusion length $\sqrt{\alpha \Delta t}$ for the one second heat source is 1.7 mm, so at distances less than this, e.g. $|R| = .05$ mm and $|R| = 0.5$ mm, the temperature responds quickly to the heat source and begins to equilibriate over the one second the heat source is enabled. At larger distances, such as $|R| = 5$ mm in Fig. 2c, the profile is dominated by the time required for diffusion. Heating is not observed until $t = 0.5$ s, a full 0.3 s after the heat source was turned on. The temperature does not peak until well after the $t = 1.2$ s turn-off time.

The overall shape of the curves is remarkably similar across the $n = 1$D, $n = 2$D, and $n = 3D$ cases. Witness for example the similarity between the green dotted $n = 2$D line at $|R| = .05$ mm (Fig. 2a) and the blue solid $n = 3$D line at $|R| = .5$ mm (Fig. 2b). The heating profiles are nearly identical despite the fact that the first comes from a difference of exponential integrals while the second comes from a difference of error functions. In other words, the heating profiles for $n = 1$D, $n = 2$D, and $n = 3$D do indeed match each other closely, but at different radii.

In vibrothermographic testing, both the source distance $|R|$ and dimensionality $n$ are unknown and position-dependent. From the measured temperature profile at a particular pixel, we will calculate both the overall heating and an effective distance $R_{\text{eff}}$, based on comparison with a combination of the $n = 2$D and $n = 3$D profiles. The scaling of $R_{\text{eff}}$ will necessarily be different depending on the actual value of $n$. While the overall amplitude and $R_{\text{eff}}$ are the most important parameters to estimate, when the signal-to-noise ratio is sufficiently high it may be possible to also estimate the dimensionality $n$.

The first step in defining the effective distance $R_{\text{eff}}$ is to nondimensionalize the equations of table 1. We substitute the dimensionless variables $\bar{R}$ for $|R|/\sqrt{4\alpha(t_2 - t_1)}$ and $\bar{t}$ for $(t - t_1)/(t_2 - t_1)$ and neglect the leading coefficients. Nondimensionalization eliminates dependence on the thermal diffusivity of the material, meaning that the algorithm being developed can be applied without requiring a-priori knowledge of the thermal diffusivity $\alpha$. The nondimensionalized expressions for temperature are given in table 2.

We can now quantify the similarity between the heating profile at $n = 2$D with the heating profiles at $n = 1$D and $n = 3$D by evaluating inner products

$$
\begin{aligned}
\bar{T}(\bar{t}) &= 0 && (\bar{t} \leq 0) \\
\bar{T}(\bar{t}) &= \left[ \operatorname{erfc}\left( \frac{\bar{R}}{\sqrt{\bar{t}}} \right) \right] && (n = 3 \text{ and } 0 < \bar{t} \leq 1) \\
\bar{T}(\bar{t}) &= \left[ \operatorname{erfc}\left( \frac{\bar{R}}{\sqrt{\bar{t}}} \right) - \operatorname{erfc}\left( \frac{\bar{R}}{\sqrt{\bar{t}-1}} \right) \right] && (n = 3 \text{ and } \bar{t} > 1) \\
\bar{T}(\bar{t}) &= \left[ -\operatorname{Ei}\left( -\frac{\bar{R}^2}{\bar{t}} \right) \right] && (n = 2 \text{ and } 0 < \bar{t} \leq 1) \\
\bar{T}(\bar{t}) &= \left[ -\operatorname{Ei}\left( -\frac{\bar{R}^2}{\bar{t}} \right) + \operatorname{Ei}\left( -\frac{\bar{R}^2}{\bar{t}-1} \right) \right] && (n = 2 \text{ and } \bar{t} > 1) \\
\bar{T}(\bar{t}) &= \left[ \Gamma\left( -0.5, -\frac{\bar{R}^2}{\bar{t}} \right) \right] && (n = 1 \text{ and } 0 < \bar{t} \leq 1) \\
\bar{T}(\bar{t}) &= \left[ \Gamma\left( -0.5, -\frac{\bar{R}^2}{\bar{t}} \right) - \Gamma\left( -0.5, \frac{\bar{R}^2}{\bar{t}-1} \right) \right] && (n = 1 \text{ and } \bar{t} > 1)
\end{aligned}
$$

Table 2: Nondimensionalized version of table 1. $\bar{R}$ represents $|R|/\sqrt{4\alpha(t_2 - t_1)}$. $\bar{t}$ represents $(t - t_1)/(t_2 - t_1)$. $\bar{T}$ represents a dimensionless quantity proportional to temperature increase.

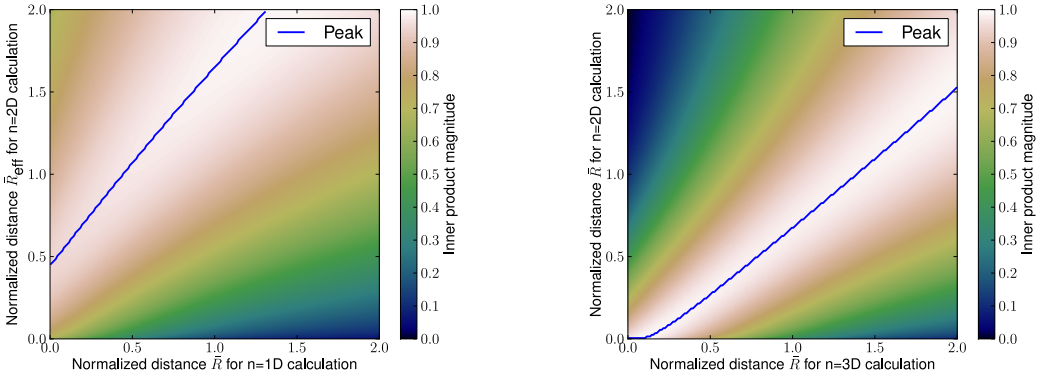


(a) 2D vs. 1D (b) 2D vs. 3D.

Figure 4: Numerical calculations of inner products between normalized time-profiles of $n$ = 2D heat conduction and (a) $n$ = 1D or (b) $n$ = 3D heat conduction. Color or intensity represents the magnitude of the inner product. A dark curve indicates the peak. Position on the horizontal axis represents actual normalized distance assuming 1D or 3D conduction. Position on the vertical axis represents the interpreted normalized distance if 2D heat conduction is assumed.

between nondimensionalized heating profiles, normalized to unit magnitude ($L_2$-norm). Figure 4 shows the inner product between the 2D heating profile and the 1D and 3D profiles as a function of normalized distance $\bar{R}$. In both cases the inner product approaches unity, indicating just how closely the heating profiles for $n = 2$D can match profiles for $n = 1$D and $n = 3$D. Based on the very close match indicated in Fig. 4, comparison by inner product with $n = 2$D heating profiles would fit most possible heating profiles.

Unfortunately, a close look at the lower left corner of Fig. 4b reveals that the $n = 2$D heating profiles are not capable of approximating the $n = 3$D profiles for $\bar{R}_{3D} < .2$. The solid curve is essentially horizontal, giving a degeneracy between $\bar{R}^{3D} = 0$ and $\bar{R}^{3D} = 0.1$ where the same 2D effective distances correspond to a range of 3D distances. This means that if we were to estimate distances by comparison with the 2D calculated profiles, normalized 3D propagation distances between 0 and 0.1 would all map to a 2D distance of 0.

To work around this problem and obtain a one-to-one mapping, instead of comparing with 2D heating profiles at all distances we will compare with 3D heating profiles at very short distances ($\bar{R}_{eff} \leq 0.2$), interpolation between 2D and 3D profiles at intermediate distances ($0.2 < \bar{R}_{eff} \leq 0.5$), and with

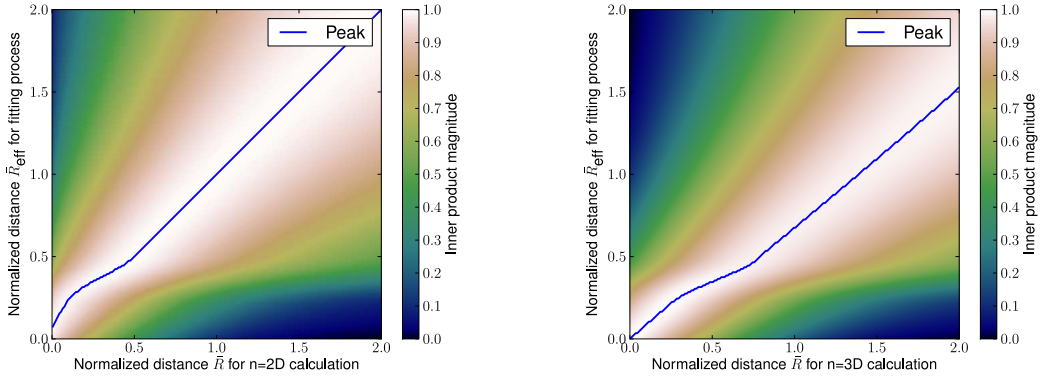


(a) Fit vs. 2D (b) Fit vs. 3D.

Figure 5: Numerical calculations of inner products between heating profiles used for fitting versus (a) $n = 2$D heat conduction. and (b) $n = 3$D heat conduction

2D profiles at longer distances ($\bar{R}_{eff} > 0.5$). The 2D and 3D profiles are mixed using raised-cosine ramps to maximize smoothness of the transition. For the same reason, in calculating the 3D profiles the 3D distance is scaled up to better match the 2D profiles. The scaling factor of 1.15 was selected by optimizing the smoothness of the transitions shown in Fig. 5.

Figure 5a shows, analogous to Fig. 4, how 2D heat conduction is interpreted through inner products with 3D profiles at short distances, with 2D profiles at long distances, and with interpolations for a transition zone in between. Figure 5b shows how 3D heat conduction is interpreted using the same fitting algorithm (the interpretation of 1D heat conduction is only minimally changed from Fig. 4a because 1D heat flow, even at zero distance, only matches normalized 2D distances above 0.5). The degeneracy (horizontal line) is eliminated, creating the desired one-to-one mapping between effective distance and actual distance for each dimensionality.

The mapping to normalized actual distances as a function of effective distance is summarized in Fig. 6a, which shows that while the mapping is different for each dimensionality case, it is one-to-one and is therefore invertible assuming the dimensionality is known. Given a measured $\bar{R}_{eff}$ and assumed dimensionality $n$, Fig. 6a gives normalized actual distance $\bar{R}$. Multiply normalized distance by $\sqrt{4\alpha(t_2 - t_1)}$ to get physical distance.

Figure 6b shows the performance of the fitting curves (3D profiles at short distances, with 2D profiles at long distances, and interpolations in between)

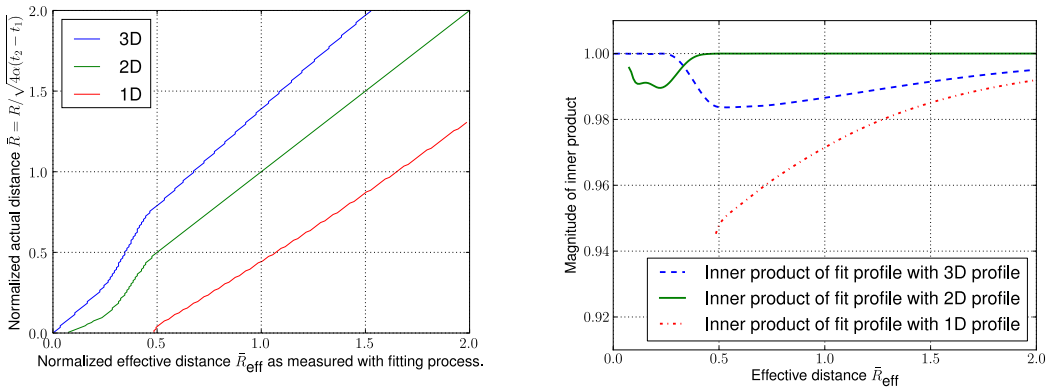


(a) (b)

Figure 6: (a) Relationship between normalized actual distances and effective distance $\bar{R}_{\text{eff}}$ (b) Magnitudes of the inner products of the fit profile with heating profiles corresponding to $n = 1$D,$n = 2$D, and $n = 3$D heat conduction. An inner product of 1.0 means that the curves are identical.

at approximating the full range of possible profiles. An inner product of 1.0 (perfect match) indicates that the fitting curve matches the profile exactly. This inner product is in all cases above .94 (and usually much higher), so the set of heating profiles used for fitting can represent each of the 1D, 2D, and 3D heating profiles almost perfectly. While they do differ slightly, a signal-to-noise of 20:1 or better will be needed to distinguish the measured profiles based on their dimensionality $n$. In contrast, the more fundamental parameters of amplitude and $\bar{R}_{\text{eff}}$ can be found even when the signal-to-noise ratio is very poor.

To summarize, we observe that the temporal heating profiles under 1D, 2D, and 3D heat propagation all have the same fundamental character, and all can be represented to 94% accuracy by a single family of profiles. This single family of heating profiles is parametrized by a normalized effective distance $\bar{R}_{\text{eff}}$, which is equivalent to $\bar{R}_{\text{3D}}/1.15$ for $\bar{R}_{\text{eff}} < .2$ and equivalent to $\bar{R}_{\text{2D}}$ for $\bar{R}_{\text{eff}} > .5$.

Physically, the n=1D and 2D heat propagation cases are spatial integrals of the 3D case. Likewise, in a vibrothermography experiment the temperature increase at any given point is the spatial integral of 3D heat flow from all points that undergo vibration-induced heating. We suggest that since this family of heating profiles can accurately approximate the $n = 1D,\ 2D,\ 3D$

| Index | Symbol | Meaning |
|---|---|---|
| 0 | $A_{\text{peak}}$ | Peak amplitude of fit |
| 1 | $\bar{R}_{\text{eff}}$ | Effective normalized distance |
| 2 | $C_{3D}$ | Coefficient of the 3D profile |
| 3 | $C_{2D}$ | Coefficient of the 2D profile |
| 4 | $C_{1D}$ | Coefficient of the 1D profile |
| 5 | $SRR$ | Signal-to-residual ratio |

Table 3: Data stored for each pixel

cases, that it will effectively parametrize the intermediate situations in vibrothermographic crack heating. Below, it is shown that experimentally observed vibrothermography heating profiles can be accurately approximated, but that a small amount of residual error does remain.

## 3. Implementation

Fitting to the heat profiles was implemented in the laboratory data acquisition software `dataguzzler` [17]. When the software acquires a new sequence of vibrothermography images, each pixel is processed independently. This consists of an initial background subtraction, followed by the curve fitting process based on the known excitation start and end times. The curve fitting process first evaluates peak amplitude and $\bar{R}_{\text{eff}}$ at each pixel, by comparison with a set of precalculated profiles and selecting the best match. It then represents the measured temperature profile based on a linear combination of 1D and 2D profiles or 2D and 3D profiles at the already determined $\bar{R}_{\text{eff}}$, yielding a "plot" with six numbers at each pixel, as listed in table 3. These numbers are combined into a hybrid false-color summary image. The process is illustrated in detail in Figs. 7 and 8. Figure 7a shows a raw infrared image of the specimen in grayscale, with crack heating superimposed using a "hot" (red-yellow) colormap. The location of the most substantial crack is marked with a white circle. The first processing step is to take the raw thermal image sequence, and subtract the background (grayscale portions of Fig. 7a) leaving only the heating (red-yellow portions of Fig. 7a).

The effective distance $\bar{R}_{\text{eff}}$ is determined for each pixel by evaluating inner products between the measured heating profile (temperature as a function of time) and normalized synthetic profiles over the range of possible $\bar{R}_{\text{eff}}$. The

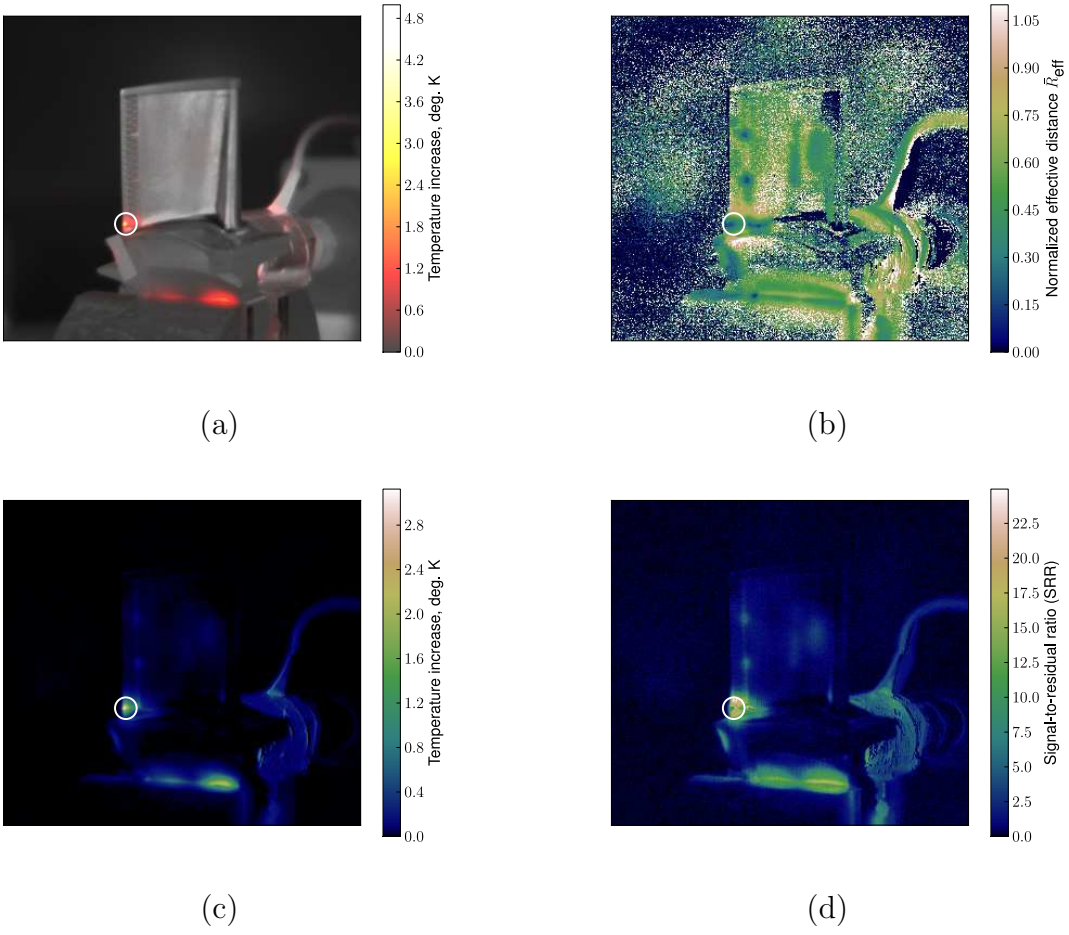


Figure 7: Vibrothermography images of a cracked turbine blade. The crack (primary indication, a few mm long) is circled. (a) Raw grayscale thermal image with crack heating colormapped. (b) Effective distance ($\log_{10} \bar{R}_{\text{eff}}$). (c) Peak amplitude. (d) Signal-to-residual ratio.

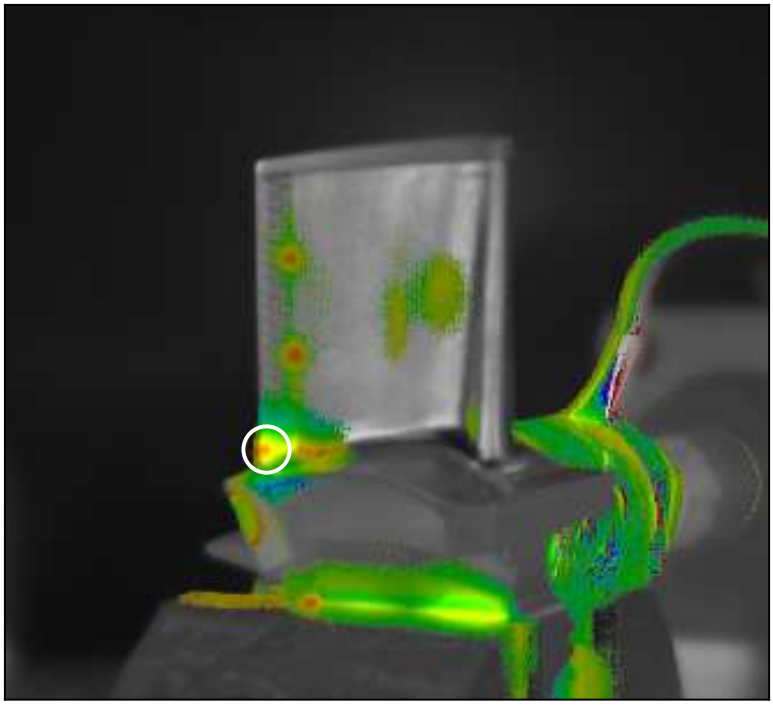

Figure 8: Processed image from Fig. 7 mapping amplitude to intensity, $\bar{R}_{\text{eff}}$ to color, and SRR to opacity over raw image.

normalized effective distance that maximizes the inner product is selected as $\bar{R}_{\text{eff}}$ and is shown in Fig. 7b. The fitting profile at this $\bar{R}_{\text{eff}}$, scaled according to the inner product, is a first approximation for the heating and cooling of this pixel across the entire sequence of images. The peak value of the profile is likewise a first approximation of the peak heating amplitude, shown in Fig. 7c. These values, $\bar{R}_{\text{eff}}$ and peak amplitude, are the two primary parameters of the fitting process. Real indications such as heat emanating from actual cracks show a radially increasing $\bar{R}_{\text{eff}}$, whereas most artifacts and false indications do not. This pattern can be seen at the circled indication and two weaker indications near the trailing edge on on Fig. 7b.

Because the fit profiles do not match theoretical heating profiles exactly (recall the inner products in Fig. 6b are not all 1.0), we attempt to both improve the potential quality of the fit and improve potential distance estimation accuracy by adding dependence on the dimensionality $n$. Remember from Fig. 6a that a given $\bar{R}_{\text{eff}}$ can map to radically different source distances. We take the inner products of each measured profile with theoretical profiles for 1D, 2D, and 3D at the measured $\bar{R}_{\text{eff}}$. We then apply bounded linear inversion (negative contributions not permitted), to represent each measured profile either as a linear combination of the 1D and 2D theoretical profiles or as a linear combination of the 2D and 3D theoretical profiles, whichever gives a better fit. The coefficients resulting from this inversion are denormalized and stored as $C_{1D}$, $C_{2D}$, and $C_{3D}$ in the plot. As coefficients of the expressions in table 2, they represent the primary means for reconstructing the measured profile from the fitted data. The improvement in the fit from allowing different dimensionality also permits a slight correction to the the peak heating amplitude $A_{\text{peak}}$.

There is always some residual error, so at each pixel signal-to-residual ratio (SRR) – defined as the $L_2$ norm of the fit over the $L_2$ norm of the residual – is calculated. Signal-to-residual ratio is a metric that describes how accurately the fitting process was able to approximate the measured heating profile, and this is the final number evaluated and stored for each pixel. It is illustrated in Fig. 7d.

The characteristic pattern of short distance surrounded by longer distance near the circled indication and two other indications near the trailing edge can be seen clearly on Fig. 7c. For most of the image the SRR (Fig. 7d) is proportional to heating amplitude because the residual is dominated by camera noise. The exception is very close to a crack where propagation is

not so well approximated by the 1D, 2D, or 3D models, limiting the SRR to around 10.

A primary benefit of this curve fitting process is the reduction of data, which both eases analysis and reduces storage requirements. The raw thermal images from a vibrothermography experiment typically include 150-200 frames which traditionally must be stepped through manually. The processing described above reduces these data to the six frames listed in table 3 plus the thermal background image. The processed data can be further reduced to a single, easy-to-interpret color image. Figure 8 shows such an image, a colorized combination of the amplitude and effective distance superimposed on top of the grayscale raw infrared background image. The effective distance $\bar{R}_{\text{eff}}$ is mapped to the hue of the colorized pixel. The peak amplitude $A_{\text{peak}}$ is mapped to the intensity (value) of the coloring. The signal-to-residual ratio is mapped both to color saturation and opaqueness of the colorized pixel over the grayscale background image. Short distances (small $|\bar{R}_{\text{eff}}|$) map to red, intermediate distances map to yellow, long distances map to green, and very long distances map to blue. Crack indications show the characteristic pattern with short distances (red or yellow) in the center surrounded by green. In contrast, apparent heating due to non-thermal artifacts, such as those caused by the specimen shifting in the grips, does not show the characteristic pattern.

The dramatic compression of data to a single image made possible by this fitting process offers the potential for automated pre-analysis that highlights possible flaws for an inspector, and pre-adjusts the contrast and thresholds. An inspector would need but a single glance per-part to see that no flaws have been found, and just a brief look to identify possible indications.

## 4. Experiments

Individual vibrothermography experiments such as the turbine blade test shown in Figs. 7 and 8 illustrate that the curve fitting/reconstruction technique described here can be useful for finding and identifying cracks. A closer look at specific pixels illustrates that, while not every detail from the physical experiment can be reproduced with this fitting process, the result is still quite accurate. Figure 9a shows raw thermal data from the hottest frame of a vibrothermography test. The crack seen here is 7.4 mm long. Figure 9b shows the same frame of the fitted reconstruction. The only observable difference is a lower background noise level in the reconstruction. Figure 9c

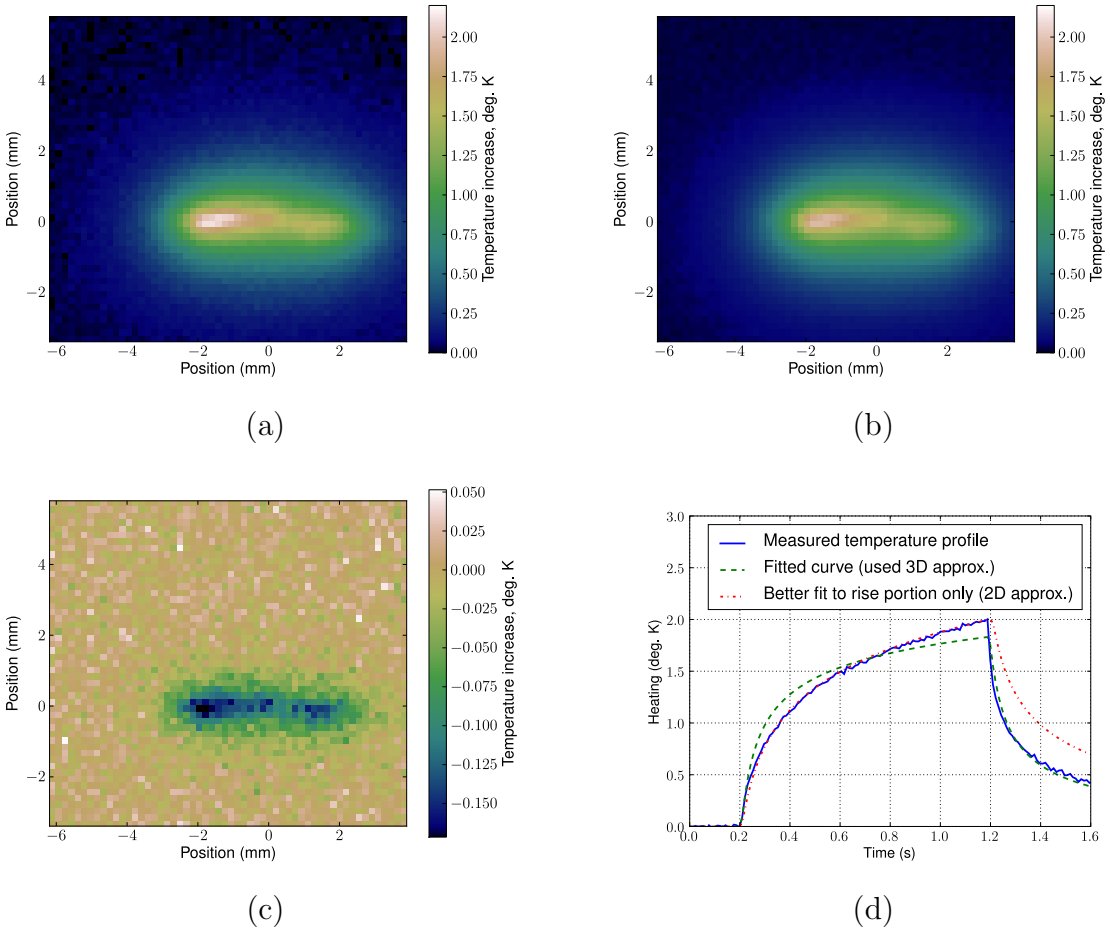


Figure 9: (a) Close-up thermal image of a crack in titanium from a vibrothermography test, just before excitation turn-off (1.19 s) (b) Corresponding reconstructed image from curve-fitted coefficients in the plot. (c) Residual error (d) Plot of temperature profile, fit, and alternative fit corresponding to the circled pixel in (c).

shows the residual fitting error of that frame. Away from the crack, fitting error is on the same order as the noise from the thermal camera ($\sigma = 22$mK). Around the crack, the fitting error of this frame, while well below 10%, shows a consistent negative bias. This is because of the particular frame chosen; other frames from the same sequence have consistent positive bias. In Fig. 9d the solid blue curve is the measured heating profile from the pixel circled in black on Fig. 9c. The fitted reconstruction of that heating profile is shown in dashed green ($n = 3$D approximation). The fit is imperfect, overestimating temperature between $t = 0.2$ and $t = 0.6$ while underestimating temperature between $t = 0.8$ and $t = 1.2$. This latter underestimate is the source of the negative bias seen in Fig. 9c.

Why is there so much error in the fit? Because the heat source distribution is not a point, line, or plane. The fitting algorithm performs a best fit to the entire profile, but more distant heat sources are more significant in the later portion of the profile than the earlier portion of the profile. From the physics of vibrothermography and geometry of this particular point we might expect heat flow to be better approximated as $n = 2$D (line-source). The dash-dot red curve in Fig. 9d shows a fit, using the rise portion only, to the 2D approximation. The fit is near near-perfect during the rise portion, but it substantially overestimates the temperature during the fall portion. The $n = 2$D approximation assumes a 1D source of infinite extent. It is not surprising that it would tend to diverge and underestimate at later times, as the finite extent of the source becomes significant. We conclude that the fidelity of the reconstruction could be improved in the future, for example by include separate fitting of the rise and fall portions of the profile. It is less clear that such an improvement would be useful, since the additional parameter would make the fitting more difficult in the most critical case where the signal-to-noise ratio is very poor. It may also make the interpretation more difficult. Another possible improvement would be to develop a better algorithm to interpolate between the $n = 1D$, $n = 2D$, and $n = 3D$ cases.

To evaluate the improvement in signal-to-noise ratio achieved by the process of fitting and reconstruction, we tried adding synthetic noise to the measured temperature profiles shown in Fig. 9, and then applying the fitting algorithm and evaluating how much synthetic noise remained. The infrared camera noise is very well approximated as zero mean, $\sigma = 22$mK additive Gaussian noise (independent and identically distributed). The synthetic noise was a factor of ten larger: Pseudorandomly generated with zero mean, $\sigma = 220$mK. Figure 10a shows the same data as 9a with this extra

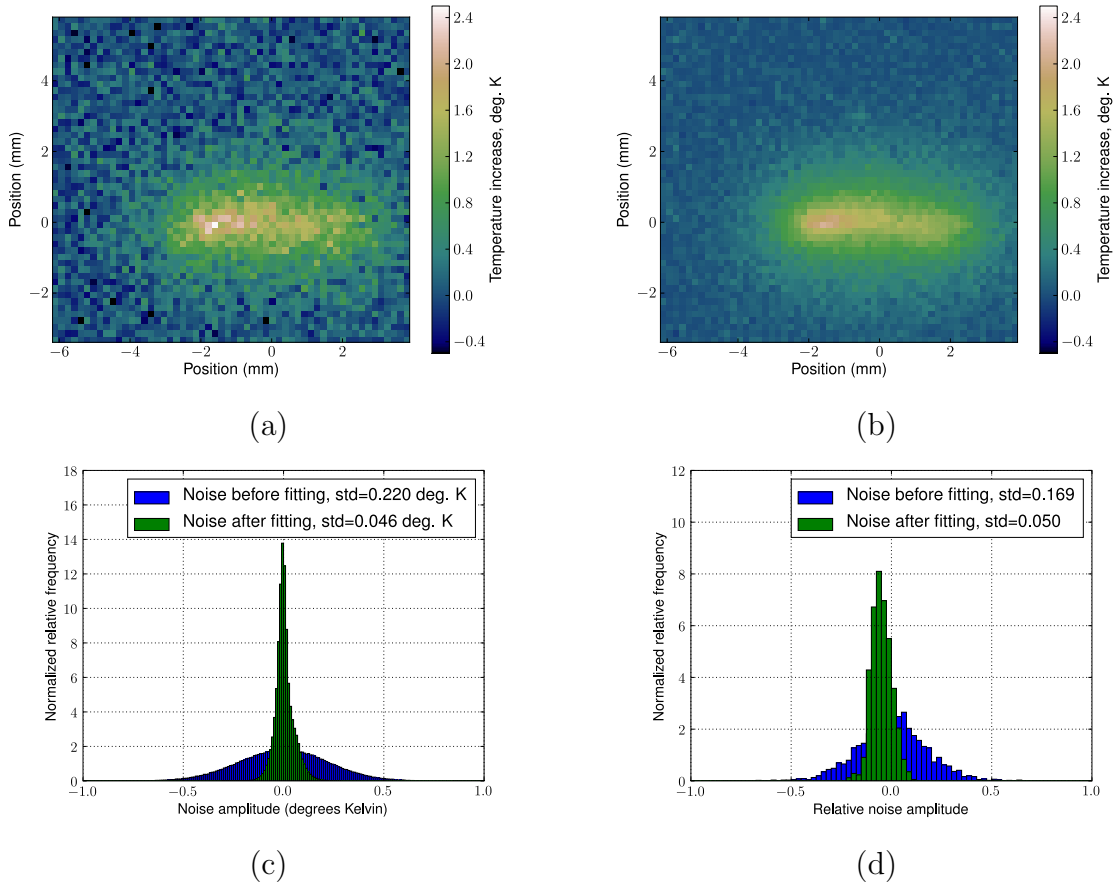


Figure 10: (a) Fig. 9a with synthetic noise added. (b) The same image reconstructed from fitted coefficients. (c) Histogram showing effect of fitting process on absolute background noise. (d) Histogram showing effect of fitting on relative foreground noise.

noise added. Figure 10b shows the result of applying the fitting algorithm to Fig. 10a. Most of the noise is removed, but the noise level remains substantially higher than in the original 9a. The noise reduction effect is quantified in Figs. 10c and 10d. For background (non-heated) pixels, absolute noise is the most relevant quantity, whereas for pixels that undergo substantial heating, relative noise (i.e. $\frac{\text{noise}}{\text{total heating}}$) is a more meaningful quantity. Figures 10c and 10d show histograms of absolute noise amplitude for the non-heating pixels and relative noise amplitude for the heating pixels respectively. These figures illustrate the reduction in noise level due to the fitting process. The background noise level in non-heating pixels is reduced from 220 mK down to 46 mK, more than a factor of four. The relative noise amplitude of pixels that are heated by the crack is reduced roughly a factor of three.

We have applied this curve fitting and image sequence reconstruction algorithm to various sets of pre-existing vibrothermography data. The results presented here are typical, in that the fitting process reduces noise and successfully compresses sequences of thermal images down to a plot that contains just a few coefficients per pixel. This algorithm does presuppose that the vibrational excitation is stationary – that it produces uniform vibration while turned on – and the data we have tested with follows that assumption. Not all vibrothermography systems generate vibration that is uniform enough to be suitable for this technique; for example some generate a startup transient followed by equilibration. Similarly, some vibrothermography systems can run in a swept-frequency mode. In that case this algorithm does not apply because the source is not stationary – the transduction of vibrational energy into heat is dependent on frequency and thus varies over time between $t_1$ and $t_2$.

## 5. Conclusions

Vibrothermographic nondestructive testing involves finding cracks by analyzing time-sequences (movies) of thermal images of vibration-induced crack heating. We have shown that the entire time-sequence can be represented as a single static plot containing just six coefficients per pixel. Of these coefficients, two – heating amplitude and effective distance – are of primary significance. Because the fit is performed with heating profiles that are calculated analytically from a-priori knowledge of the theory of heat conduction, relatively few fitting parameters are required and thus a better fit is obtained than would otherwise be possible. As a result the fitting process filters out

most noise – because noise does not fit the calculated profiles – thereby improving sensitivity to faint indications. The fitting process gives measures of heating amplitude and source distance at each pixel. The coefficients in the plot are suitable for automatic pattern recognition, and they can also be combined into a false color image that compresses the entire thermal image sequence into a single, easy-to-interpret summary.

## References


[1] K. L. Reifsnider, E. G. Henneke, W.W. Stinchcomb, "The Mechanics of Vibrothermography", in *Mechanics of Nondestructive Testing*, ed. W. W. Stinchcomb (Plenum Press, New York) (1980) 249–276.

[2] M. Morbidini, P. Cawley, T. Barden, D. Almond, and P. Duffour, Prediction of the thermosonic signal from fatigue cracks in metals using vibration damping measurements, J. Appl. Phys **100** (2006) 104905.

[3] L.D. Favro, X. Han, Z. Ouyang, G. Sun, H. Sui, and R.L. Thomas, Infrared imaging of defects heated by a sonic pulse, Rev. Sci. Instr. **71**(6) (2000) 2418-2421.

[4] X. Maldague, *Theory and Practice of Infrared Technology for Nondestructive Testing* , John Wiley and Sons, New York (2001).

[5] M. Li, S. D. Holland, W.Q. Meeker Statistical methods for automatic crack detection based on vibrothermography sequence-of-images data, Appl. Stochastic Models Bus. Ind. **26** 481–495 (2010).

[6] X. Han, L.D. Favro, Z. Ouyang, and R.L. Thomas, Recent Developments in Thermosonic Crack Detection, Review of Progress in Quantitative Nondestructive Evaluation **20** 552–557 (2002).

[7] M. Morbidini and P. Cawley, The detectability of cracks using sonic IR, J. Appl. Phys **105** 093530 (2009).

[8] M. Li, S.D. Holland, and W.Q. Meeker, Quantitative multi-inspection-site comparison of probability of detection for vibrothermography nondestructive evaluation data, in press, J. Nondestruct. Eval. (2011). `http://dx.doi.org/10.1007/s10921-011-0105-9`

[9] S. D. Holland and J. Renshaw, Physics-based image enhancement for infrared thermography, NDT&E International **43** 440-445 (2010).

[10] F. Ruhge and P. Zombo, Siemens Perspective, Presentation at the Sonic IR Working Group Meeting, QNDE 2008, University of Illinois at Chicago, July 21, 2008.

[11] Y. Guo and F. R. Ruhge, Comparison of detection capability for acoustic thermography, visual inspection, and fluorescent penetrant inspection on gas turbine components, Review of Progress in Quantitative Nondestructive Evaluation **28** 1848–1854 (2009).

[12] X. Maldague and S. Marinetti, Pulse phase infrared thermography, J. Appl. Phys **79**(5) 2694–2698 (1996).

[13] S. M. Shepard, J. R. Lhota, B. A. Rubadeux, D. Wang, and T. Ahmed, Reconstruction and enhancement of active thermographic image sequences, Opt. Eng. **42**(5) 1337-1342 (2003).

[14] J. Renshaw, S. D. Holland, and R. B. Thompson, Measurement of crack opening stresses and crack closure stress profiles from heat generation in vibrating cracks, Appl. Phys. Lett **93** 081914 (2008).

[15] J. V. Beck, K. D. Cole, A. Haji-Sheikh, and B. Litkouhi, *Heat Conduction Using Green's Functions*, Taylor & Francis, 1992.

[16] Wolfram Research, Wolfram Mathematica Online Integrator, `http://integrals.wolfram.com/`.

[17] S. D. Holland, *Dataguzzler* data acquisition software `http://thermal.cnde.iastate.edu/dataguzzler/`.

## 6. Acknowledgements

This material is based upon work supported by the Air Force Research Laboratory under Contract #FA8650-04-C-5228 at Iowa State University's Center for NDE.